RESEARCH ARTICLE | JULY 10 2025

Conductivity space isotherm behavior in quantum anomalous Hall devices

N. T. M. Tran ; V. Ortiz Jimenez ; M. Musso ; L. K. Rodenbach ; M. P. Andersen ; H. M. Hill ; P. Zhang; L. Tai ; K. L. Wang ; M. Marzano ; M. Ortolano ; D. B. Newell; C. A. Richter; A. F. Rigosi

AIP Advances 15, 075023 (2025)
https://doi.org/10.1063/5.0278373

Conductivity space isotherm behavior in quantum anomalous Hall devices

Cite as: AIP Advances 15, 075023 (2025); doi: 10.1063/5.0278373
Submitted: 29 April 2025 • Accepted: 24 June 2025 •
Published Online: 10 July 2025

View Online Export Citation CrossMark

N. T. M. Tran,[1,2] V. Ortiz Jimenez,[1] M. Musso,[3] L. K. Rodenbach,[4,5] M. P. Andersen,[5,6] H. M. Hill,[1] P. Zhang,[7] L. Tai,[7] K. L. Wang,[7] M. Marzano,[8] M. Ortolano,[3] D. B. Newell,[1] C. A. Richter,[1] and A. F. Rigosi[1,a)]

AFFILIATIONS

[1] Physical Measurement Laboratory, National Institute of Standards and Technology (NIST), 100 Bureau Drive, Gaithersburg, Maryland 20899-8171, USA
[2] Joint Quantum Institute, University of Maryland, College Park, Maryland 20742, USA
[3] Department of Electronics and Telecommunications, Politecnico di Torino, Torino 10129, Italy
[4] Department of Physics, Stanford University, Stanford, California 94305, USA
[5] Stanford Institute for Materials and Energy Sciences, SLAC National Accelerator Laboratory, Menlo Park, California 94025, USA
[6] Department of Materials Science and Engineering, Stanford University, Stanford, California 94305, USA
[7] Department of Electrical Engineering, University of California, Los Angeles, California 90095, USA
[8] Istituto Nazionale di Ricerca Metrologica, Torino 10135, Italy

[a)] **Author to whom correspondence should be addressed:** albert.rigosi@nist.gov

ABSTRACT

The quantum Hall effect (QHE) has enhanced accessibility to measure and disseminate electrical units, owed in part to the recently redefined International System of Units in 2019. Graphene remains one of the preferred options to realize the ohm despite the limitations of high magnetic fields to produce a robust QHE. Topological insulators, on the other hand, show promise in providing quantized resistance via the quantum anomalous Hall effect, a phenomenon that removes the need for magnetic fields during operation. To optimize future devices for metrological applications, it is important to gain a better understanding of magnetically doped topological insulators like Cr-doped bismuth antimony telluride. The application of differential conductivity space analyses offers a more sensitive way to analyze the data and distinguish between 2D and 3D transport behaviors. This is particularly important in thin films, where the transition between 2D and 3D behavior can be subtle. The ability to confidently determine the dimensionality of the transport is crucial for selecting appropriate theoretical models for future device optimization. Furthermore, this work identifies variable range hopping as the dominant transport mechanism in the 2D regime using a rigorous statistical analysis (via the Bayes factor). These elements assist in the understanding of microscopic processes that govern charge transport in these materials.

Magnetically doped topological insulators (MTIs) offer access to the quantum anomalous Hall effect (QAHE), a phenomenon that corresponds to time-reversal symmetry breaking and the presence of an energy gap that can harbor topological surface states.[1–3] In the context of physics and metrology, these robust QAHE states have the potential to replace the modern usage of the corresponding integer quantum Hall effect plateaus in graphene-based technology on the merits that the QAHE does not require ongoing operation of a magnetic field to provide quantized resistance. Historically, realizing the unit of electrical resistance (the ohm) with graphene has been made more user-friendly by means of simplifying equipment infrastructure and increasing device shelf-life.[4–13]

One avenue for substantially reducing equipment infrastructure needs is to implement a resistance standard that can operate without an electromagnet.[14–16] Though this may be possible with systems such as chromium doped bismuth antimony telluride,[17,18]

there are still various physical behaviors that need to be incorporated more efficiently in future devices, most pertinently in the realm of quantum transport. As with conventional quantum Hall physics, one metric that can reveal QAHE transition behavior is the conductivity, which frequently manifests itself as a dissipationless current closely associated with the two quantization conditions $\sigma_{yx} = e^2/h$ and $\sigma_{xx} = 0$. Therefore, any metrics that can more efficiently determine device behavior, namely to distinguish between 2D and 3D transport regimes and identify the dominant transport mechanisms, would be of utmost utility in the metrological application of these material systems.

In this work, such metrics are introduced after collecting resistivity measurements and conducting analyses of the conductivity space of the h/e^2 ($\nu = 1$) transition in $Cr_{0.12}(Bi_{0.26}Sb_{0.62})_2Te_3$ (where $\frac{h}{e^2} \equiv R_K \approx 25.8$ kΩ). The conductivity isothermal curve behavior is determined by means of analyzing transport data as a function of temperature, gate voltage, and magnetic field. An inspection of the differential conductivities shows that the devices exhibit strong characteristics of a 2D transport regime driven by conventional variable range hopping, and this model is further supported by a rigorous statistical analysis via Bayes factor comparison. Such analyses may be applied to any QAHE-exhibiting system, even when results may not be globally applicable to all topological insulators. With more efficient methods of understanding observed electrical behaviors and mechanisms of transport, MTI-based devices could be more optimally fabricated or grown, allowing one to pursue metrological applications related to the quantum ampere.[19–21]

The MTI material used herein was grown in a PerkinElmer ultra-high-vacuum molecular beam epitaxy system.[22,23] Six quintuple layers of high-quality single-crystalline Cr-doped $(Bi_xSb_{1-x})_2Te_3$ film [where $x = 0.26$, to obtain $Cr_{0.12}(Bi_{0.26}Sb_{0.62})_2Te_3$] were grown on a semi-insulating GaAs (111)B substrate after a pre-anneal step of 630 °C in a Te-rich environment to remove native oxides, with the final resulting film measuring ~6 nm in thickness. During the growth process, the GaAs substrate temperature was maintained at 200 °C with the Bi, Sb, Te, and Cr sources all evaporating nearly simultaneously. The material thickness was monitored by reflection high-energy electron diffraction, and once the growth was complete, the sample was removed from the chamber and coated with a layer of polymethyl methacrylate for surface protection.

The fabrication of MTI-based devices began with direct-write optical photolithography, and each patterning step included the coating of a hexamethyldisilazane adhesion layer and a Megaposit SPR 3612 photoresist layer (see Acknowledgments) along with a pre-exposure bake at 80 °C for 120 s. The photoresist layer was then exposed to 385 nm LED ultraviolet light with a dose of ~100 mJ/cm^2 and then developed in a 1:1 solution of Microposit CD-30:H_2O for 35 s. The Hall bar device geometry was defined via argon ion milling. The electrical contact pads were composed of a 5 nm Ti adhesion layer and a 90 nm Au layer, both deposited via electron beam evaporation after a 10 s *in situ* Ar pre-etch removed surface impurities. For top gate implementation, a dielectric layer of 1 nm of Al was deposited as a seed layer. This thin layer was oxidized before depositing about 40 nm of Al_2O_3 with atomic layer deposition using trimethylaluminum and water precursors. Finally, a deposition of 5 nm Ti and 80 nm Au completed the top gate.

Test devices were measured in two different setups, the first being a Bluefors dilution refrigerator from its base temperature of 10 mK to ~2 K and magnetic field capabilities of up to 14 T (see Acknowledgments). The second system is a Physical Property Measurement System (PPMS) from Quantum Design with the base temperature of 1.6–400 K and magnetic field up to 14 T (see Acknowledgments). The JCC-28 sample holder accommodates shielded wiring that externally connects to a Q-Devil breakout box for the Bluefors and a custom-made breakout box for the PPMS. Measurements were collected with a set of lock-in amplifiers for both systems.

To center the Fermi level within the magnetic exchange gap of the MTI-based device, the longitudinal resistivity (ρ_{xx}, and generally equal to $(w/l) \times \{|R_{K+xx}| - |R_K|\}$, where w and l are the width and length of the device, respectively, and R_K is the von Klitzing constant from earlier) was monitored as a function of gate voltage. Optimal placement, manifesting as a global minimum in the resistance of a longitudinal pair of electrical contacts, enables the most robust access to the QAHE. As shown in Figs. 1(a) and 1(b), the device was fabricated to allow for measuring both longitudinal and Hall resistances simultaneously using a 50 nA electrical current across the source and drain terminals. All data were collected by modifying three parameters: (1) gate voltage, which ranged from −0.3 to

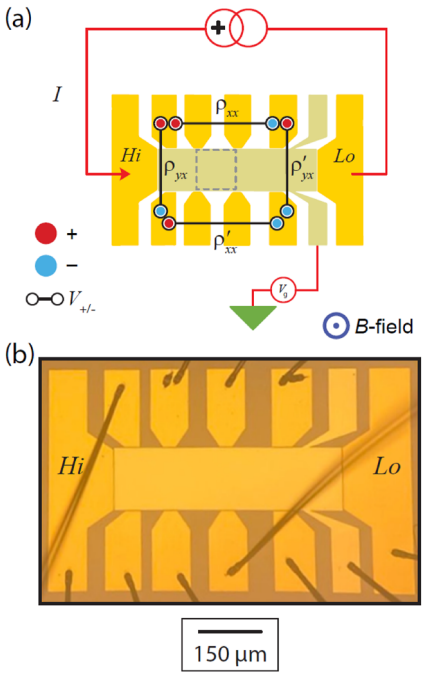

FIG. 1. (a) An illustration of the device design is shown, with a basic layout of the measurement configuration. Resistance is measured between longitudinal (ρ_{xx}) and Hall contact pairs (ρ_{yx}). The gray dotted square highlights the equal spacing between longitudinal and Hall contact pairs, with the device having a width of 150 μm. Magnetic field direction is also provided by the indicator in the lower right corner. (b) An optical image of the device is provided along with a scale bar.

−8 V to maintain proximity to the magnetic exchange gap, (2) temperature, which was changed in steps of 0.1 K below 1 K, 1 K below 10 K, and 10 K below 100 K, and (3) magnetic field, which was swept in both directions to fully record hysteresis.

The highest quality device required a gate voltage of about −1.9 V to provide a robust QAHE with minimal longitudinal resistance (see the supplementary material). Of the several pairs of orthogonal contacts, the highest quality pair, determined by the deviation of the resistance from the nominal value of the $\nu = 1$ plateau (~25.8 kΩ), was subsequently used for a more in-depth analysis of the hysteresis curves present in the magnetic-field-dependent Hall resistance. Figures 2(a)–2(c) document a series of Hall resistances (R_{yx}) measured as a function of magnetic field for several gate voltages. The long-dashed lines start at −5 T and increase, and the short-dotted lines start at 5 T and decrease. These resistances are also measured as a function of temperature, as indicated by the color-coded gradient (up to 30 K). To obtain a metric for assessing the persistence of the QAHE state, one may use the change in magnetic field needed to switch the magnetization (defined as ΔB). This value may be extracted where R_{yx} intercepts zero, giving an effective width to the hysteresis loop. Figure 3 discusses this analysis in more depth.

Before discussing the aforementioned metric, one should observe that high-quality QAHE quantization can withstand slightly higher temperatures when the gate voltage is near the middle of the magnetic exchange gap (−1.9 V) than if the gate voltage is not centered. The hysteresis loops also enclose a smaller area for higher temperatures. As one drifts farther from the gap [−0.3 V, Fig. 2(c)], the hysteresis loops' enclosed areas decrease more rapidly with temperature, and the QAHE plateau begins to lose its flat profile at higher magnetic fields. Both of the effects are even more exaggerated

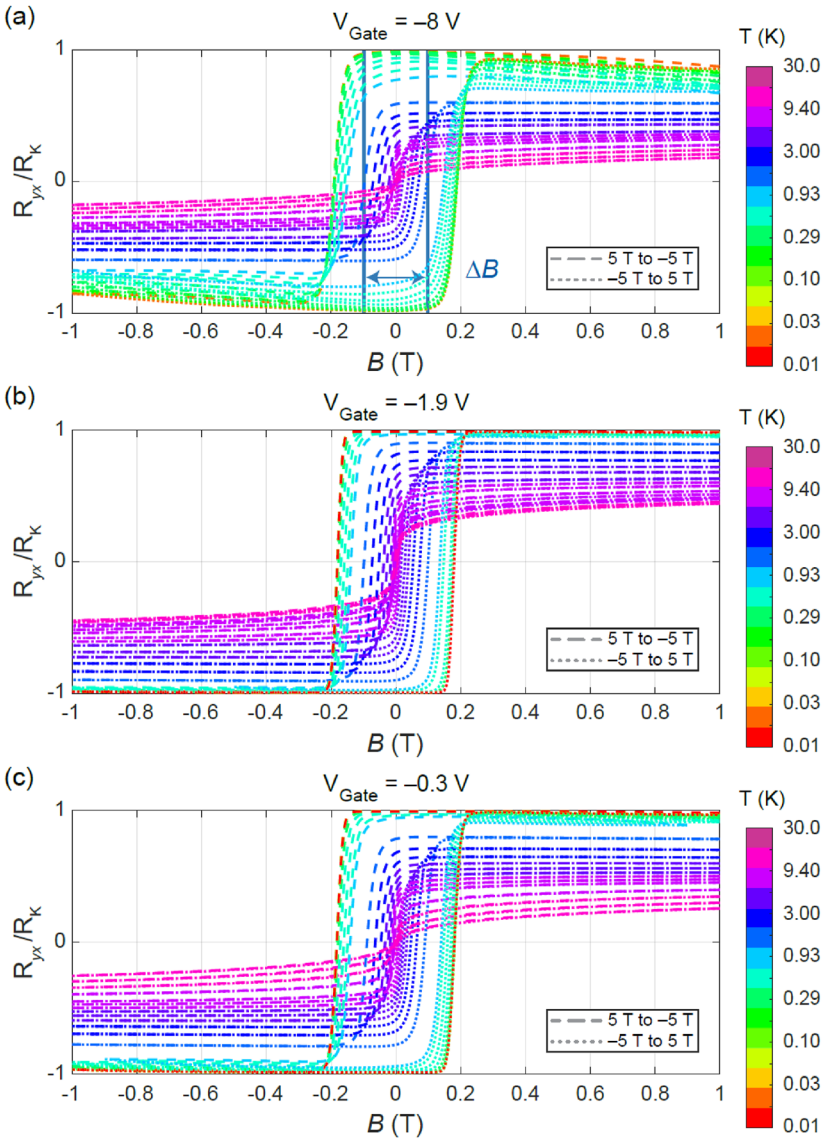

FIG. 2. Hall resistance is examined as a function of magnetic field for both sweeping directions, where the long-dashed lines start at −5 T and increase, and the short-dotted lines start at 5 T and decrease. The following gate voltages were used: (a) −8 V, (b) −1.9 V, and (c) −0.3 V. In all cases, data for temperatures up to 30 K are shown. Panel (a) also shows a visualization of the metric ΔB, which characterizes the gap in magnetic field present when switching the direction of magnetization in the device.

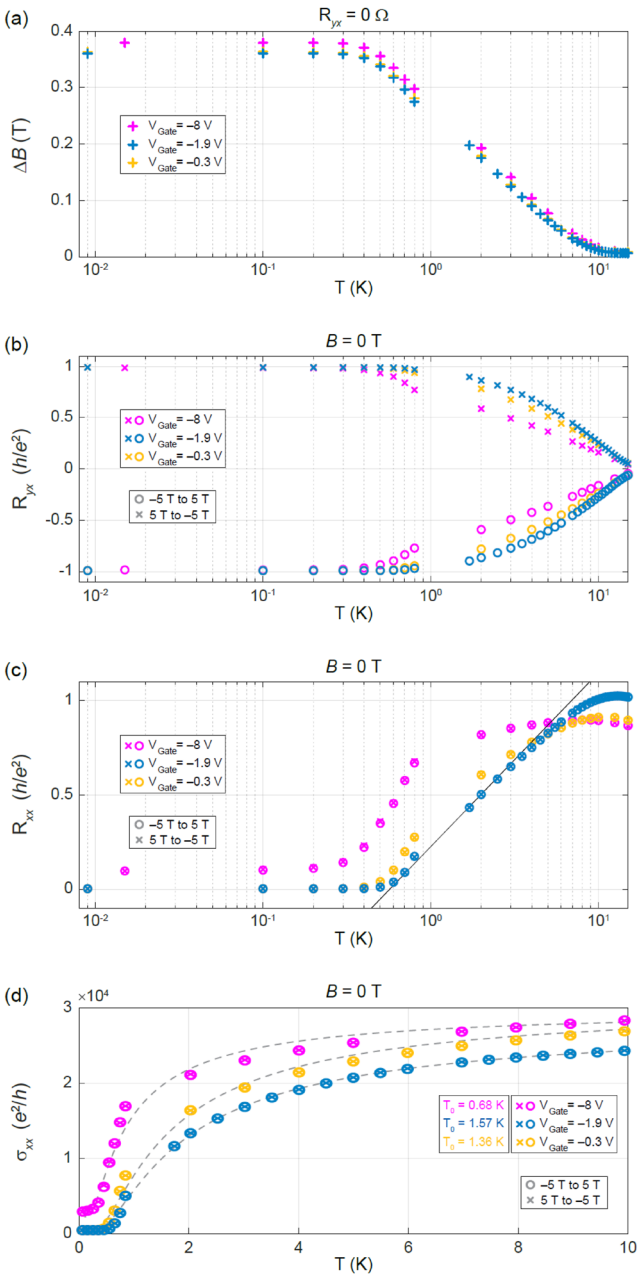

FIG. 3. (a) The metric ΔB, as described in Fig. 2(a), is plotted for the same temperature scale to suppose a dual temperature regime picture observed in the resistance data. The magnetic field values are taken from the point when the Hall resistance is zero. (b) The Hall resistance values at zero magnetic field are plotted as a function of temperature on a semi-logarithmic scale. Three gate voltages are included (−8, −1.9, and −0.3 V in magenta, dark blue, and orange, respectively). The data support the dual regime picture and exhibit behavior with a common convergence point near 10 K. (c) The longitudinal resistance values are plotted as a function of temperature on a semi-logarithmic scale using the same gate voltages. The data show two linear regimes that cross near 0.6 K. (d) Arrhenius fits, shown as dashed gray curves, using the same gate voltages, are performed to extract temperature scales for thermal activation of conduction.

in Fig. 2(a), where the gate voltage of −8 V was used and is farthest from the gap. By returning to the metric ΔB, as described in Fig. 2(a), which is plotted in Fig. 3(a) on a semi-logarithmic temperature scale, a dual temperature regime emerges. The magnetic field values are taken from the point when the Hall resistance is zero, and the metric vanishes by about 10 K. This metric also shows two prominent linear trends (again, on a semi-logarithmic plot) with a crossover temperature near 0.6 K.

Tracking R_{yx} and R_{xx} supports this dual regime picture within which the quality of the quantization takes on different temperature-dependent behaviors. For instance, by analyzing R_{yx} in Fig. 3(b), one sees that the QAHE retains its flat profile until about 1 K (within the magnetic exchange gap). Moreover, the point at which R_{yx} vanishes, about 10 K, appears to be a common point of convergence for every gate voltage. The differences in the curve profiles for each of the gate voltages between about 1 and 10 K may possibly stem from the varying number of available states in the bands just above and below the magnetic exchange gap.[14] When one looks carefully at Fig. 3(c), the dual regime picture is clearer for R_{xx}. The first regime sees a flat R_{xx} up until a point of inflection or crossover near 0.6 K for the optimal gate voltage, aligned with the observation of the metric ΔB. Above that temperature, an exponential trend characterizes the increase of the longitudinal resistance (linear on the semi-logarithmic plots). A possible third regime, though less defined in its crossover point, occurs as the temperature approaches 10 K, where a more asymptotic behavior is exhibited.

To understand if the crossover near 0.6 K corresponds to any observable changes in the device's conductivity, two pairs of R_{xx} and R_{yx} resistance data were collected as a function of magnetic field in both sweeping directions. Many traditional works focused on the quantum Hall effect (QHE) have used conductivity space to learn more about transitions in the material.[24–38] Therefore, this approach was taken for this material system. To calculate σ_{xx} and σ_{xy} for transforming resistivity data, the following equations were used:

$$\sigma_{xx} = \frac{\rho_{xx}}{{\rho_{xx}}^2 + {\rho_{yx}}^2} \quad and \quad \sigma_{xy} = \frac{-\rho_{yx}}{{\rho_{xx}}^2 + {\rho_{yx}}^2}. \tag{1}$$

The longitudinal conductivity allows one to gain insight into the effect of thermal activation via Arrhenius fitting, as performed in Fig. 3(d) via $\sigma_{xx} = a + be^{T_0/T}$. Here, a and b are constants and T_0 characterizes a temperature scale on which the effects of thermal activation are expected to be observable and significant on the conductivity.[39] In the same figure, gray dashed curves are used to superimpose the fits on the data and allow for the extraction of three temperature scales depending on the gate voltage. For the optimal gate voltage (−1.9 V), the relevant scale, T_0, is about 1.57 K. The behavior of the other two values of T_0, that is, 0.68 and 1.36 K for −8 and −0.3 V, respectively, behaves in a similar manner to those reported in similar work.[39] In short, the parameter T_0 increases until the optimal gate voltage and then begins decreasing again. This observation highlights the sensitivity of the robustness of σ_{xx} for MTI-based devices for modest changes in gate voltage.

Moving forward with the full conductivity space analysis, when one combines the geometrical features of the device design with the measurement results, the values of ρ_{xx} are straightforwardly determinable. Furthermore, an average of the two pairs for the ρ_{xx} and

ρ_{yx} was calculated to symmetrize the data. This analysis, performed for all applied gate voltages, yielded the conductivity space isothermal curves in Figs. 4(a)–4(c), reflecting gate voltages of −8, −1.9, and −0.3 V, respectively. Two features immediately stand out: (1) a dimpled feature that forms in the isotherm below a certain temperature and (2) a general contraction and expansion along the vertical of the isotherms as a function of temperature, with the optimal gate voltage [(b)] exhibiting the greatest compression and strongest dimple formation.

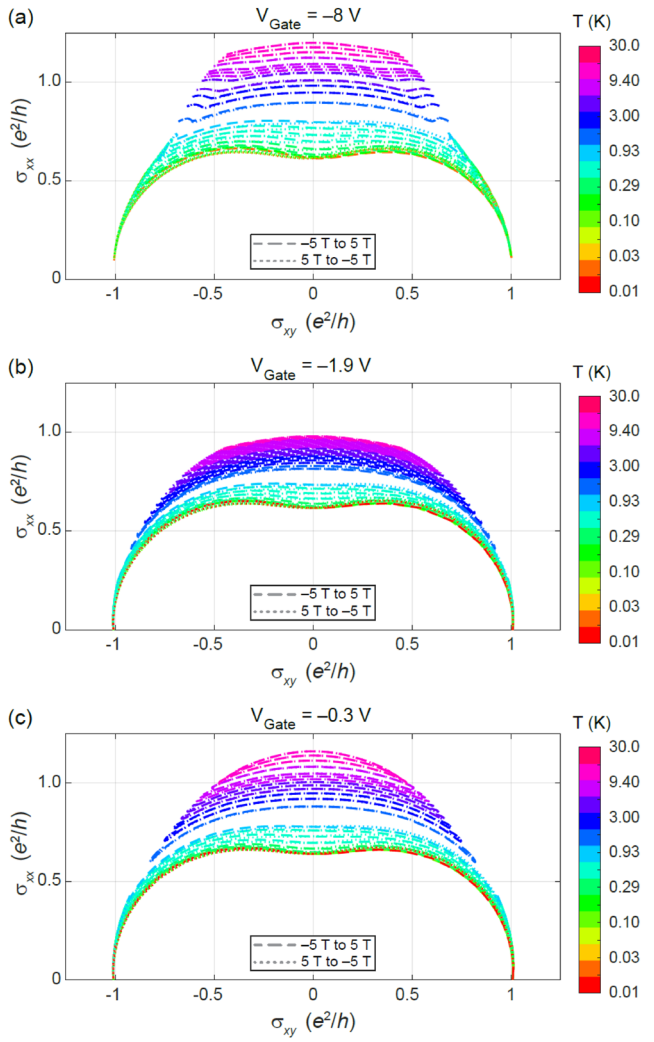

FIG. 4. Conductivity space isothermal curves were calculated based on resistivity values for the device exhibited between −5 and 5 T and at temperatures between 10 mK and 30 K. The long-dashed lines represent datasets that begin at −5 T and increase, whereas the short-dotted lines represent datasets that begin at 5 T and decrease. The following gate voltages were used: (a) −8, (b) −1.9, and (c) −0.3 V. The most immediate observations show two features: (1) a dimpled feature that forms in the isotherm below a certain temperature and (2) a general contraction and expansion along the vertical of the isotherms as a function of temperature, with the optimal gate voltage [(b)] exhibiting the greatest compression and strongest dimple formation.

Most of the isothermal curves in Fig. 4 follow an elliptical shape not unlike those associated with semicircular domain boundaries typically seen in gallium arsenide, graphene and, more recently, in MTI-based devices.[30–45] As mentioned earlier, it appears that as temperature decreases, the elliptical shape of an isothermal curve flattens until a crossover point, below which a dimple forms in the center of the curve. The dimple sharpens as the temperature gets to the lowest value of ~10 mK. As seen in vanadium-doped MTI-based devices,[42] the ideal case scenario would show this dimple sharpening into a cusp, reflecting the 2D nature of the material system.[43]

The 6 nm thickness of this chromium-doped MTI-based device should comfortably classify it within the 2D picture reported by Ref. 42 rather than the 3D axion insulator behavior seen in thicker films (films that exhibit axion insulation can be as thin as 9 nm). In this case, due to the lack of sharp cusp normally expected,[43] one cannot yet confidently treat the transport behaviors as 2D. To resolve this issue, one may analyze how the isothermal curves deform with temperature and then compare this overall behavior with that of a different MTI-based device or material system.

To get a more pronounced representation of the deforming, a method for better revealing subtle changes in isothermal curve shapes was used; namely, by taking the first derivative of the plots, $\frac{d\sigma_{xx}}{d\sigma_{xy}}$. When processing the data, 100-point adjacent averaging was applied to obtain a smoother function for differentiation. An example of this analysis is shown in Figs. 5(a) and 5(b) for the optimal gate voltage of −1.9 V. From these derivatives, one may define a metric for mathematically determining when the dimple feature vanishes, namely "Δ," or the relative vertical measure of the two local extrema. This metric will be important for comparing this material system to another to help justify the use of 2D transport models and also may allow one to neglect issues arising from any 3D representation of the material system.

For simpler viewing of the data in Figs. 5(a) and 5(b), the magnetic field sweeps are separated as (a) beginning at −5 T and increasing and (b) beginning at 5 T and decreasing. Furthermore, a subset of the temperature scale is selected since Δ remains zero above 1 K. For each of the three gate voltages used in previous figures, Δ can be seen plotted against temperature in Figs. 5(c) and 5(d). One notable observation, as indicated by the solid light blue region up to ~0.2 K, involves a clear separation of two temperature ranges where Δ either remains stable (below 0.2 K) or commences its decrease to zero (between 0.2 and 0.8 K), or the threshold value at which dimpled features arise.

To gain better insight into the benefits of using the derivatives on these isothermal curves, additional analyses are conducted in the supplementary material, mainly by reviewing the case for vanadium-doped MTI-based devices.[42] Two main comparisons emerge: (1) the trend for Δ is similar in form to what is reported here for the chromium-doped material system, and (2) the symmetry of the isothermal curves with respect to the central dimple or cusp exists for both systems (and both are classified as 2D by the metrics of Ref. 42).

To strengthen confidence in the usefulness of the derivatives as a means to indicate the extent to which an MTI-based device fits a 2D regime picture, temperature-dependent conductivity data were analyzed in the same fashion presented here for a vanadium-doped device with a thickness of 7.3 nm (see the supplementary material). The characteristics of the isothermal curves reveal the

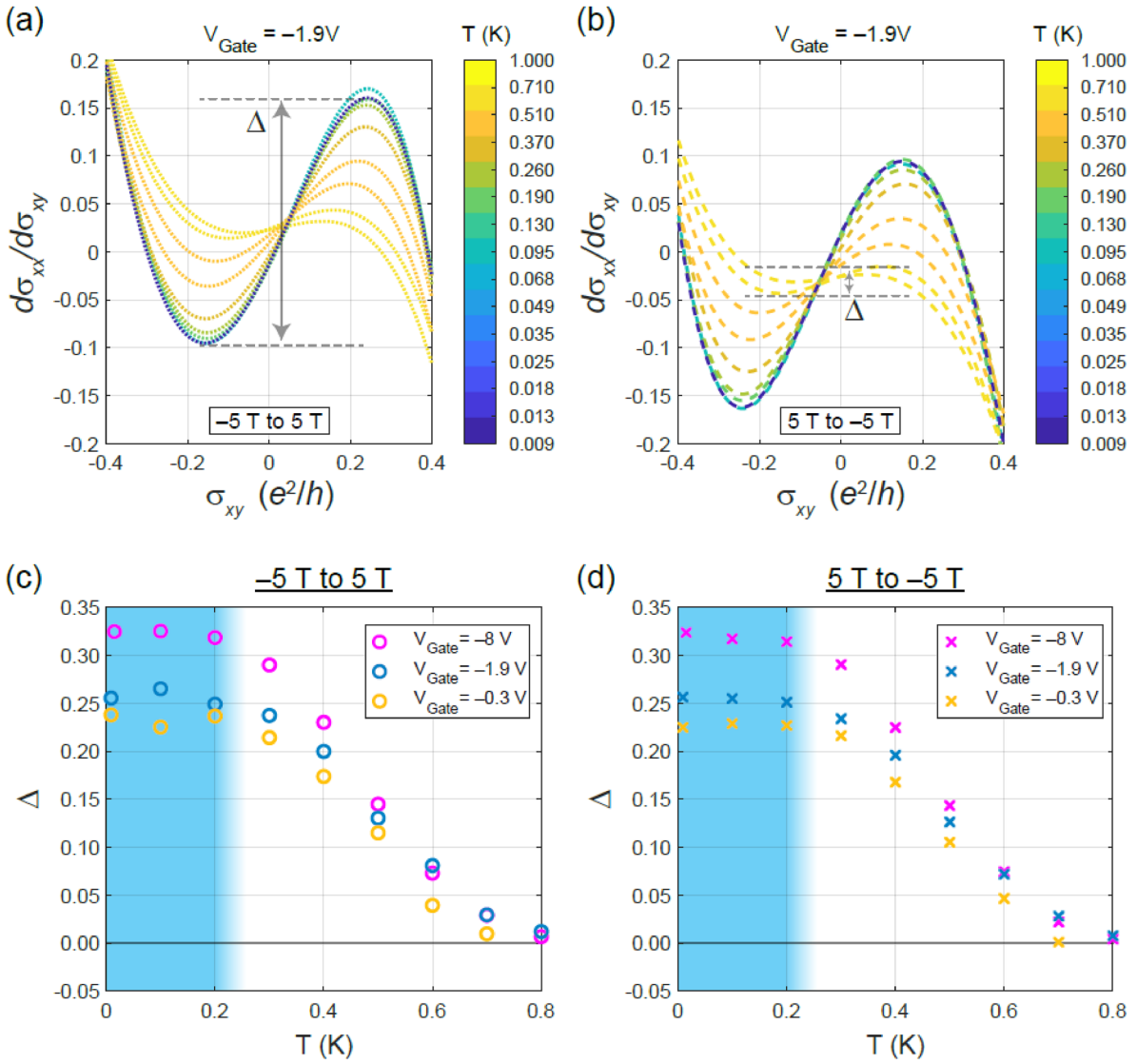

FIG. 5. All data from Fig. 3 were differentiated after applying adjacent averaging to enhance the subtle feature of dimple formation within the isothermal curves. Since the magnetic field sweep direction imposes a minor translation in the data, the sweeps are separated as (a) beginning at −5 T and increasing and (b) beginning at 5 T and decreasing. A subset of the temperature scale is selected since the metric of interest, Δ, vanishes above 1 K. (c)–(d) Δ, defined as the relative vertical measure of the two local extrema, is calculated from the derivatives as a function of temperature for both magnetic field sweep directions and for three gate voltages. The solid light blue region up to ~0.2 K indicates the approximate temperature range where Δ remains stable relative to the range up to 0.8 K.

3D nature of the system, specifically the non-centered positioning of the dimple/cusp feature with higher temperature and the asymmetric expansion of one-half of the isothermal curve as temperature increases (details provided in the supplementary material). The conductivity derivative analysis has thus provided a more efficient and pronounced way of determining the appropriateness of using 2D or 3D transport models.

Returning to Figs. 5(c) and 5(d), the point at which Δ begins to decrease, in the neighborhood of 0.2 K, may be attributable to thermal activation, variable range hopping, phonon-assisted (field-driven) hopping, or bootstrap electron heating (BSEH), as described in Ref. 14. The reason a phenomenon like BSEH is not being considered is because such a model was used to explain current-dependent breakdown both in the QAHE and the conventional quantum Hall effect.[14,40,41] In short, the BSEH model attributes a sharp change in resistivity to runaway heating of the electron system when the current exceeds about 100 nA, prompting this experiment to use electric currents below that threshold. In addition, at higher temperatures

like 0.2 K, the breakdown transition due to BSEH is expected to be smeared out.[14]

It has been noted that in the neighborhood where Δ begins to decrease and approach 0, MTI-based devices may see discrepancies of σ_{xx} when fit against a thermal activation model, suggesting that another transport mechanism was required for resolution; thus, any choice of transport models made here was guided by the physical characteristics of the system and by evidence of appropriateness in the literature.[14,44] Since only surface states can contribute to transport (given that the device is comfortably in the 2D regime), variable range hopping (VRH) and potentially VRH with field-driven (FD) hopping may be the most appropriate models to help explain the trends in longitudinal conductivity at zero-field, and they are both represented by Eqs. (2) and (3), respectively,

$$\sigma_{xx}(T) = \sigma_{xx}^{T} e^{-(T_1/T)^{\alpha}}, \tag{2}$$

$$\sigma_{xx}(I_x, T) = \sigma_{xx}^{T} exp\left[\frac{eE_y a}{k_B T} - \left(\frac{T_1}{T}\right)^{\alpha}\right]. \tag{3}$$

For Eqs. (2) and (3), σ_{xx}^{T} is a prefactor with little temperature dependence compared to the T_1 constant, or characteristic temperature scale reported for these models, and the constant α is defined as $1/(1+d)$, where d is the number of spatial dimensions,[14] noting that the definition is different than that posed in Ref. 1 for a similar analysis of VRH. The elementary charge, e, and the orthogonal field strength while the device exhibits a full QAHE, E_y, in Eq. (3) are part of the term in the exponent meant to incorporate field-driven (or phonon-assisted) transport. In Fig. 6, data for the longitudinal conductivities as a function of temperature are plotted along with the two models per gate voltage. The VRH and VRH+FD models are shown as a long-dashed curve and a dotted curve, respectively (and the fit parameters are shown in the supplementary material and are generally consistent with the literature for chromium-doped devices[14]). Since both models differ for each spatial dimension, the 2D and 3D forms of α were used. The case where α = 1/2 (or 1 spatial dimension) is shown in the supplementary material but is not a common finding as described in other work.[14,45]

Even if one focuses on the assumption that the 6 nm thick devices are purely in the 2D regime, it is not entirely clear which model is more appropriate, and this lack of clarity has been reported elsewhere for chromium-doped devices.[14] To better understand which model may statistically describe the data more satisfactorily, a Bayes factor analysis was also conducted on the two models,[46,47] much of which is reported in the supplementary material. In summary, the analysis compares the marginal likelihood integral (MLI) of each model, which is a metric representing the fit of the model to its corresponding dataset. The Bayes factor is then calculated as a ratio of the MLIs of the two models being compared. Generally, when the Bayes factor is greater than 100 (or if the logarithm of the Bayes factor is much greater than 5), the model of interest (in this case, the VRH model) is statistically more appropriate than the alternative model (VRH+FD). Any smaller factor would suggest little mathematical justification for utilizing the VRH model (model of interest). The analysis showed that the logarithm Bayes factor comparing VRH to VRH+FD is much greater than 5 (for −1.9 V, it is ~600), strongly supporting the VRH model over the VRH+FD model.

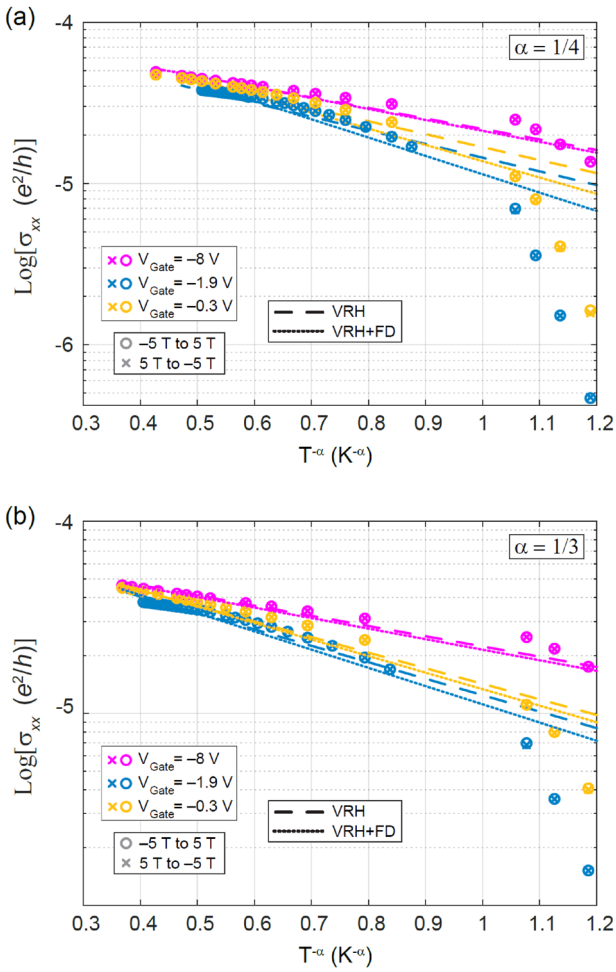

FIG. 6. Temperature dependent longitudinal conductivity data at zero magnetic field for each of the three gate voltages are plotted. Zero field is selected to maximize focus on thermal contributions to on ohmic variable range hopping (VRH). After determining the dimensionality via dimple/cusp behavior earlier, the next step to understanding electrical measurements is to determine the dominant transport mechanism. Two models are used to fit the data based on VRH and a combination of VRH and field-driven (FD) hopping, shown as a long-dashed curve and a dotted curve, respectively. Both models differ for each spatial dimension, with (a) α = 1/4 (or 3 spatial dimensions) and (b) α = 1/3 (or 2 spatial dimensions). The case of α = 1/2 (or 1 spatial dimension) is shown in the supplementary material but is not a common finding as described in other work.[14,45]

To better support the notion that the 2D transport is dominated by the VRH model, a secondary analysis is shown in the supplementary material for temperatures at the extreme end of the model, namely below 0.8 K. This secondary analysis also supports this designation. The entire assessment of 2D transport was enabled and more easily achievable by using Δ and the derivatives of conductivity as a proxy for intuiting that the material system was comfortably in the 2D regime as opposed to the 3D axion insulator regime. Combined with the rigorous Bayes factor statistical

analysis, these subtle mathematical insights highlight the utility of characterizing MTI-based devices in conductivity space.

This work described resistivity measurement results and analyses of the conductivity space of the h/e^2 (ν = 1) transition in $Cr_{0.12}(Bi_{0.26}Sb_{0.62})_2Te_3$. When measuring a device of relatively similar composition (Cr-based) but not exactly the same as others in the recent literature (V-based like Ref. 42), then it is safe to say one cannot initially be 100 % certain if a 2D or 3D transport model is more appropriate. This statement is also most reasonable to state even when the stoichiometries are different within the same dopant class of material. However, for this particular work, Cr and V dopants are essentially being compared. Reference 42 was heavily relied upon to conclude that the system in this work is not purely 3D because the physics of axion insulators, independent of dopant, prohibits a dimple from forming at the origin, and a dimple forms quite clearly at lower temperatures for the system in this work.

Therefore, the system is either purely 2D or a hybrid 2D/3D system. Although it was initially thought, prior to the growth, that a 6 nm sample would make any device certainly 2D, Fig. 4 shows behavior that resembles a hybrid device when compared to V-doped stoichiometries. Specifically, the dimple/cusp did not sharply return to the origin as with pure 2D systems at similarly cold temperatures. It was then concluded that this discrepancy warranted investigation in this work, including how to consider the possibility that we may have a hybrid 2D/3D system despite the 6 nm thickness. To answer the question of whether this material system was more hybrid or more purely 2D, V-doped data were analyzed in the supplementary material and found that hybrid systems exhibit a temperature-dependent asymmetry with their isothermal curves. Because the main device data did not exhibit that asymmetry with temperature, one could reasonably estimate that our system was a pure 2D system. To further support this assertion, the presented derivatives analysis was used to more easily reveal the different temperature regimes that could reflect different transport mechanisms exclusive to 2D electron physics. The utilization of Bayes factor analysis confirmed, with significant statistical backing, that the Variable Range Hopping model is most appropriate to use for this system. The knowledge now acquired gives one information that could be used in a feedback loop with theoretical calculations or different material growth parameters for future device property optimization.

See the supplementary material for a gate voltage sweep, an image of example devices, trends in external vanadium-doped devices, fitting parameter details, and the Bayes factor analysis.

The authors would like to acknowledge S. Mhatre, M. Munoz, and E. C. Benck for their assistance in the NIST internal review process, as well as D. Goldhaber-Gordon for fruitful discussions. The authors also acknowledge support by the Department of Energy, Office of Science, Basic Energy Sciences, Materials Sciences and Engineering Division, under Contract No. DE-AC02-76SF00515. Work presented herein was performed, for a subset of the authors, as part of their official duties for the United States Government. Funding is hence appropriated by the United States Congress directly. The authors declare no competing interests.

Commercial equipment, instruments, and materials are identified in this paper in order to specify the experimental procedure adequately. Such identification is not intended to imply recommendation or endorsement by the National Institute of Standards and Technology or the United States Government, nor is it intended to imply that the materials or equipment identified are necessarily the best available for the purpose.

AUTHOR DECLARATIONS

Conflict of Interest

The authors have no conflicts to disclose.

Author Contributions

N.T.M.T. and V.O.J. contributed equally to this work.

N. T. M. Tran: Conceptualization (equal); Data curation (equal); Formal analysis (lead); Validation (equal); Visualization (equal); Writing – original draft (lead); Writing – review & editing (lead). **V. Ortiz Jimenez**: Conceptualization (equal); Data curation (equal); Formal analysis (lead); Validation (equal); Visualization (equal); Writing – original draft (lead); Writing – review & editing (lead). **M. Musso**: Conceptualization (equal); Data curation (equal); Formal analysis (equal); Writing – original draft (equal); Writing – review & editing (equal). **L. K. Rodenbach**: Methodology (equal); Resources (equal); Writing – review & editing (equal). **M. P. Andersen**: Methodology (equal); Resources (equal); Writing – review & editing (equal). **H. M. Hill**: Formal analysis (supporting); Writing – original draft (equal); Writing – review & editing (equal). **P. Zhang**: Methodology (equal); Resources (equal); Writing – review & editing (equal). **L. Tai**: Methodology (equal); Resources (equal); Writing – review & editing (equal). **K. L. Wang**: Methodology (equal); Resources (equal); Writing – review & editing (equal). **M. Marzano**: Supervision (equal); Writing – review & editing (equal). **M. Ortolano**: Supervision (equal); Writing – review & editing (equal). **D. B. Newell**: Project administration (equal); Supervision (equal); Writing – original draft (equal); Writing – review & editing (equal). **C. A. Richter**: Project administration (equal); Supervision (equal); Writing – original draft (equal); Writing – review & editing (equal). **A. F. Rigosi**: Conceptualization (lead); Data curation (equal); Formal analysis (lead); Methodology (lead); Project administration (lead); Supervision (lead); Visualization (equal); Writing – original draft (lead); Writing – review & editing (lead).

DATA AVAILABILITY

The data that support the findings of this study are available from the corresponding author upon reasonable request.

REFERENCES

[1] C. Z. Chang, J. Zhang, X. Feng, J. Shen, Z. Zhang, M. Guo, K. Li, Y. Ou, P. Wei, L. L. Wang, Z. Q. Ji *et al.*, "Experimental observation of the quantum anomalous Hall effect in a magnetic topological insulator," Science **340**, 167 (2013).

[2] Y. L. Chen, J.-H. Chu, J. G. Analytis, Z. K. Liu, K. Igarashi, H.-H. Kuo, X. L. Qi, S. K. Mo, R. G. Moore, D. H. Lu, M. Hashimoto, T. Sasagawa, S. C. Zhang, I. R. Fisher, Z. Hussain, and Z. X. Shen, "Massive Dirac fermion on the surface of a magnetically doped topological insulator," Science **329**, 659 (2010).

[3]J. G. Checkelsky, J. Ye, Y. Onose, Y. Iwasa, and Y. Tokura, "Dirac-fermion-mediated ferromagnetism in a topological insulator," Nat. Phys. **8**, 729 (2012).
[4]A. Tzalenchuk, S. Lara-Avila, A. Kalaboukhov, S. Paolillo, M. Syväjärvi, R. Yakimova, O. Kazakova, T. J. B. M. Janssen, V. Fal'Ko, and S. Kubatkin, "Towards a quantum resistance standard based on epitaxial graphene," Nat. Nanotechnol. **5**, 186 (2010).
[5]R. Ribeiro-Palau, F. Lafont, J. Brun-Picard, D. Kazazis, A. Michon, F. Cheynis, O. Couturaud, C. Consejo, B. Jouault, W. Poirier, and F. Schopfer, "Quantum Hall resistance standard in graphene devices under relaxed experimental conditions," Nat. Nanotechnol. **10**, 965 (2015).
[6]D. G. Jarrett, C.-C. Yeh, S. U. Payagala, A. R. Panna, Y. Yang, L. Meng, S. M. Mhatre, N. T. M. Tran, H. M. Hill, D. Saha, R. E. Elmquist, D. B. Newell, and A. F. Rigosi, "Graphene-based star-mesh resistance networks," IEEE Trans. Instrum. Meas. **72**, 1502710 (2023).
[7]M. Woszczyna, M. Friedemann, M. Götz, E. Pesel, K. Pierz, T. Weimann, and F. J. Ahlers, "Precision quantization of Hall resistance in transferred graphene," Appl. Phys. Lett. **100**, 164106 (2012).
[8]A. R. Panna, I.-F. Hu, M. Kruskopf, D. K. Patel, D. G. Jarrett, C.-I. Liu, S. U. Payagala, D. Saha, A. F. Rigosi, D. B. Newell, C.-T. Liang, and R. E. Elmquist, "Graphene quantum Hall effect parallel resistance arrays," Phys. Rev. B **103**, 075408 (2021).
[9]M. Kruskopf, S. Bauer, Y. Pimsut, A. Chatterjee, D. K. Patel, A. F. Rigosi, R. E. Elmquist, K. Pierz, E. Pesel, M. Götz, and J. Schurr, "Graphene quantum Hall effect devices for AC and DC electrical metrology," IEEE Trans. Electron Devices **68**, 3672 (2021).
[10]T. J. B. M. Janssen, S. Rozhko, I. Antonov, A. Tzalenchuk, J. M. Williams, Z. Melhem, H. He, S. Lara-Avila, S. Kubatkin, and R. Yakimova, "Operation of graphene quantum Hall resistance standard in a cryogen-free table-top system," 2D Mater. **2**, 035015 (2015).
[11]D. S. Scaletta, S. M. Mhatre, N. T. M. Tran, C. H. Yang, H. M. Hill, Y. Yang, L. Meng, A. R. Panna, S. U. Payagala, R. E. Elmquist, D. G. Jarrett, D. B. Newell, and A. F. Rigosi, "Optimization of graphene-based quantum Hall arrays for recursive star–mesh transformations," Appl. Phys. Lett. **123**, 153504 (2023).
[12]A. F. Rigosi and R. E. Elmquist, "The quantum Hall effect in the era of the new SI," Semicond. Sci. Technol. **34**, 093004 (2019).
[13]H. He, K. H. Kim, A. Danilov, D. Montemurro, L. Yu, Y. W. Park, F. Lombardi, T. Bauch, K. Moth-Poulsen, T. Iakimov, R. Yakimova *et al.*, "Uniform doping of graphene close to the Dirac point by polymer-assisted assembly of molecular dopants," Nat. Commun. **9**, 3956 (2018).
[14]E. J. Fox, I. T. Rosen, Y. Yang, G. R. Jones, R. E. Elmquist, X. Kou, L. Pan, K. L. Wang, and D. Goldhaber-Gordon, "Part-per-million quantization and current-induced breakdown of the quantum anomalous Hall effect," Phys. Rev. B **98**, 075145 (2018).
[15]Y. Okazaki, T. Oe, M. Kawamura, R. Yoshimi, S. Nakamura, S. Takada, M. Mogi, K. S. Takahashi, A. Tsukazaki, M. Kawasaki, Y. Tokura, and N.-H. Kaneko, "Precise resistance measurement of quantum anomalous Hall effect in magnetic heterostructure film of topological insulator," Appl. Phys. Lett. **116**, 143101 (2020).
[16]M. Götz, K. M. Fijalkowski, E. Pesel, M. Hartl, S. Schreyeck, M. Winnerlein, S. Grauer, H. Scherer, K. Brunner, C. Gould, F. J. Ahlers, and L. W. Molenkamp, "Precision measurement of the quantized anomalous Hall resistance at zero magnetic field," Appl. Phys. Lett. **112**, 072102 (2018).
[17]L. K. Rodenbach, A. R. Panna, S. U. Payagala, I. T. Rosen, M. P. Andersen, P. Zhang, L. Tai, K. L. Wang, D. G. Jarrett, R. E. Elmquist, D. B. Newell, D. Goldhaber-Gordon, and A. F. Rigosi, "Metrological assessment of quantum anomalous Hall properties," Phys. Rev. Appl. **18**, 034008 (2022).
[18]Y. Okazaki, T. Oe, M. Kawamura, R. Yoshimi, S. Nakamura, S. Takada, M. Mogi, K. S. Takahashi, A. Tsukazaki, M. Kawasaki, Y. Tokura, and N.-H. Kaneko, "Quantum anomalous Hall effect with a permanent magnet defines a quantum resistance standard," Nat. Phys. **18**, 25–29 (2021).
[19]M. W. Keller and J. Aumentado, "A new era for the ampere," Physics **9**, 144 (2016).
[20]H. Scherer and B. Camarota, "Quantum metrology triangle experiments: A status review," Meas. Sci. Technol. **23**, 124010 (2012).
[21]Y. Tang, V. N. Ojha, S. Schlamminger, A. Rüfenacht, C. J. Burroughs, P. D. Dresselhaus, and S. P. Benz, "A 10 V programmable Josephson voltage standard and its applications for voltage metrology," Metrologia **49**, 635 (2012).
[22]X. Kou, S. T. Guo, Y. Fan, L. Pan, M. Lang, Y. Jiang, Q. Shao, T. Nie, K. Murata, J. Tang, Y. Wang, L. He, T. K. Lee, W. L. Lee, and K. L. Wang, "Scale-invariant quantum anomalous Hall effect in magnetic topological insulators beyond the two-dimensional limit," Phys. Rev. Lett. **113**, 137201 (2014).
[23]A. J. Bestwick, E. J. Fox, X. Kou, L. Pan, K. L. Wang, and D. Goldhaber-Gordon, "Precise quantization of the anomalous Hall effect near zero magnetic field," Phys. Rev. Lett. **114**, 187201 (2015).
[24]H. P. Wei, D. C. Tsui, and A. M. M. Pruisken, "Localization and scaling in the quantum Hall regime," Phys. Rev. B **33**, 1488 (1986).
[25]A. M. M. Pruisken, "Universal singularities in the integral quantum Hall effect," Phys. Rev. Lett. **61**, 1297 (1988).
[26]C. P. Burgess, R. Dib, and B. P. Dolan, "Derivation of the semicircle law from the law of corresponding states," Phys. Rev. B **62**, 15359 (2000).
[27]C. P. Burgess and B. P. Dolan, "Quantum Hall effect in graphene: Emergent modular symmetry and the semicircle law," Phys. Rev. B **76**, 113406 (2007).
[28]L.-I. Huang, Y. Yang, C.-W. Liu, R. E. Elmquist, S.-T. Lo, F.-H. Liu, and C.-T. Liang, "Unusual renormalization group (RG) flow and temperature-dependent phase transition in strongly-insulating monolayer epitaxial graphene," RSC Adv. **7**, 31333 (2017).
[29]Y. Xue and E. Prodan, "Quantum criticality at the Chern-to-normal insulator transition," Phys. Rev. B **87**, 115141 (2013).
[30]X. Kou, L. Pan, J. Wang, Y. Fan, E. S. Choi, W. L. Lee, T. Nie, K. Murata, Q. Shao, S. C. Zhang, and K. L. Wang, "Metal-to-insulator switching in quantum anomalous Hall states," Nat. Commun. **6**, 8474 (2015).
[31]J. G. Checkelsky, R. Yoshimi, A. Tsukazaki, K. S. Takahashi, Y. Kozuka, J. Falson, M. Kawasaki, and Y. Tokura, "Trajectory of the anomalous Hall effect towards the quantized state in a ferromagnetic topological insulator," Nat. Phys. **10**, 731 (2014).
[32]M. Liu, W. Wang, A. R. Richardella, A. Kandala, J. Li, A. Yazdani, N. Samarth, and N. P. Ong, "Large discrete jumps observed in the transition between Chern states in a ferromagnetic topological insulator," Sci. Adv. **2**, e1600167 (2016).
[33]M. Mogi, M. Kawamura, R. Yoshimi, A. Tsukazaki, Y. Kozuka, N. Shirakawa, K. S. Takahashi, M. Kawasaki, and Y. Tokura, "A magnetic heterostructure of topological insulators as a candidate for an axion insulator," Nat. Mater. **16**, 516 (2017).
[34]M. Mogi, M. Kawamura, A. Tsukazaki, R. Yoshimi, K. S. Takahashi, M. Kawasaki, and Y. Tokura, "Tailoring tricolor structure of magnetic topological insulator for robust axion insulator," Sci. Adv. **3**, eaao1669 (2017).
[35]D. Xiao, J. Jiang, J. H. Shin, W. Wang, F. Wang, Y. F. Zhao, C. Liu, W. Wu, M. H. Chan, N. Samarth, and C. Z. Chang, "Realization of the axion insulator state in quantum anomalous Hall sandwich heterostructures," Phys. Rev. Lett. **120**, 056801 (2018).
[36]M. Kawamura, M. Mogi, R. Yoshimi, A. Tsukazaki, Y. Kozuka, K. S. Takahashi, M. Kawasaki, and Y. Tokura, "Topological quantum phase transition in magnetic topological insulator upon magnetization rotation," Phys. Rev. B **98**, 140404 (2018).
[37]L. Pan, X. Liu, Q. L. He, A. Stern, G. Yin, X. Che, Q. Shao, P. Zhang, P. Deng, C. Y. Yang, B. Casas, E. S. Choi, J. Xia, X. Kou, and K. L. Wang, "Probing the low-temperature limit of the quantum anomalous Hall effect," Sci. Adv. **6**, eaaz3595 (2020).
[38]D. Zhuo, Z. J. Yan, Z. T. Sun, L. J. Zhou, Y. F. Zhao, R. Zhang, R. Mei, H. Yi, K. Wang, M. H. W. Chan, C. X. Liu *et al.*, "Axion insulator state in hundred-nanometer-thick magnetic topological insulator sandwich heterostructures," Nat. Commun. **14**, 7596 (2023).
[39]I. T. Rosen, M. P. Andersen, L. K. Rodenbach, L. Tai, P. Zhang, K. L. Wang, M. A. Kastner, and D. Goldhaber-Gordon, "Measured potential profile in a quantum anomalous Hall system suggests bulk-dominated current flow," Phys. Rev. Lett. **129**, 246602 (2022).
[40]S. Komiyama and Y. Kawaguchi, "Heat instability of quantum Hall conductors," Phys. Rev. B **61**, 2014 (2000).

[41]S. Komiyama, T. Takamasu, S. Hiyamizu, and S. Sasa, "Breakdown of the quantum Hall effect due to electron heating," Solid State Commun. **54**, 479 (1985).
[42]K. M. Fijalkowski, N. Liu, M. Hartl, M. Winnerlein, P. Mandal, A. Coschizza, A. Fothergill, S. Grauer, S. Schreyeck, K. Brunner, M. Greiter *et al.*, "Any axion insulator must be a bulk three-dimensional topological insulator," Phys. Rev. B **103**, 235111 (2021).
[43]S. Grauer, K. M. Fijalkowski, S. Schreyeck, M. Winnerlein, K. Brunner, R. Thomale, C. Gould, and L. W. Molenkamp, "Scaling of the quantum anomalous Hall effect as an indicator of axion electrodynamics," Phys. Rev. Lett. **118**, 246801 (2017).
[44]M. Kawamura, R. Yoshimi, A. Tsukazaki, K. S. Takahashi, M. Kawasaki, and Y. Tokura, "Current-driven instability of the quantum anomalous Hall effect in ferromagnetic topological insulators," Phys. Rev. Lett. **119**, 016803 (2017).
[45]M. Furlan, "Electronic transport and the localization length in the quantum Hall effect," Phys. Rev. B **57**, 14818 (1998).
[46]D. J. Dunstan, J. Crowne, and A. J. Drew, "Easy computation of the Bayes factor to fully quantify Occam's razor in least-squares fitting and to guide actions," Sci. Rep. **12**, 993 (2022).
[47]D. J. C. MacKay, "A practical Bayesian framework for backpropagation networks," Neural Comput. **4**, 448 (1992).